Aeroelastic Characterization of a Flexible Wing Using Particle Tracking Velocimetry Measurements

Mertens, C.; de Rojas Cordero, T.; Sodja, J.; Sciacchitano, A.; van Oudheusden, B.W.

DOI
10.2514/1.J060713

Publication date
2022

Document Version
Final published version

Published in
AIAA Journal: devoted to aerospace research and development

Citation (APA)
Mertens, C., de Rojas Cordero, T., Sodja, J., Sciacchitano, A., & van Oudheusden, B. W. (2022). Aeroelastic Characterization of a Flexible Wing Using Particle Tracking Velocimetry Measurements. *AIAA Journal: devoted to aerospace research and development*, *60*(1), 276-286. https://doi.org/10.2514/1.J060713

AIAA JOURNAL
Vol. 60, No. 1, January 2022

Aeroelastic Characterization of a Flexible Wing Using Particle Tracking Velocimetry Measurements

Christoph Mertens,* Tomás de Rojas Cordero,† Jurij Sodja,‡ Andrea Sciacchitano,§ and Bas W. van Oudheusden¶
Delft University of Technology, 2629 HS Delft, The Netherlands

https://doi.org/10.2514/1.J060713

The aerodynamic, elastic, and inertial components in Collar's triangle of forces acting on a flexible wing with span width $s = 1.75$ m and chord $c = 0.25$ m are determined based on integrated optical measurements of the structural and aerodynamic response to steady and unsteady periodic inflow conditions at a chord-based Reynolds number of 2.3×10^5. The measurement device is a coaxial volumetric velocimeter mounted on a robotic arm, which is used to perform optical measurements of fiducial markers on the wing surface, and helium-filled soap bubbles, which are used as flow tracers. The optical measurements of the structural markers and the flow tracers are both processed with the Lagrangian particle tracking algorithm Shake-the-Box. Subsequently, physical models are used to determine the inertial and elastic forces of the aeroelastic interaction from the marker tracking results, and to determine the unsteady aerodynamic lift force from the flow velocity fields. The results of this integrated aeroelastic characterization approach are in physical agreement with each other according to the equilibrium of forces in Collar's triangle and good agreement with external reference measurements.

Nomenclature

A	=	aerodynamic force, N
c	=	chord length, m
D'	=	drag per unit span, N/m
E	=	elastic force, N
EI	=	flexural rigidity, N/m^2
e	=	Euler's number
$\boldsymbol{f}$	=	finite element external load vector
f_g	=	gust frequency, Hz
f_s	=	sampling frequency, Hz
h	=	height, m
I	=	inertial force, N
I'	=	inertial force per unit span, N/m
i	=	imaginary unit
$\boldsymbol{K}$	=	stiffness matrix
k	=	reduced frequency
L'	=	lift per unit span, N/m
M	=	bending moment in the beam, N · m
$\boldsymbol{M}$	=	mass matrix
Q	=	shear force in the beam, N
q	=	external load on the beam, N/m
s	=	span width, m
T	=	period of the gust excitation, s
t	=	time, s
U_∞	=	freestream velocity, m/s
$\boldsymbol{u}$	=	flow velocity vector
w	=	out-of-plane deflection, m
α	=	geometric angle of incidence of the wing, deg
β	=	angle of gust vanes, deg
Γ_b	=	bound circulation, m^2/s
Γ_p	=	partial circulation, m^2/s
γ	=	bound vortex sheet strength, m/s
δ	=	force measurement residual, N
ε	=	relative measurement residual
ε	=	strain
μ	=	mass per unit span, kg/m
$\boldsymbol{\xi}$	=	finite element model degree-of-freedom vector
ρ	=	fluid density, kg/m^3
σ	=	standard deviation
φ	=	phase lag, rad
ω_g	=	angular frequency of the gust, rad/s

Subscripts

a	=	amplitude of the dynamic forcing/response
0	=	steady (part of the) forcing/response

Presented as Paper 2021-0221 at the AIAA Scitech 2021 Forum, Virtual Event, 11–15 & 19–21 January 2021; received 15 March 2021; revision received 20 May 2021; accepted for publication 9 June 2021; published online Open Access 16 August 2021.

*Ph.D. Student, Aerodynamics Department, Faculty of Aerospace Engineering; C.Mertens@tudelft.nl (Corresponding Author).

†M.Sc. Student, Aerodynamics Department, Faculty of Aerospace Engineering; currently GE Renewable Energy, Barcelona, Spain.

‡Senior Researcher, Aerospace Structures and Materials Department, Faculty of Aerospace Engineering. Member AIAA.

§Assistant Professor, Aerodynamics Department, Faculty of Aerospace Engineering.

¶Associate Professor, Aerodynamics Department, Faculty of Aerospace Engineering.

I. Introduction

A POPULAR concept to depict the field of aeroelasticity and categorize the problems that occur within it is Collar's triangle of forces (see Fig. 1), introduced by Collar [1]. This schematic represents graphically the interaction of the three forces involved in aeroelasticity, which are the aerodynamic, elastic, and inertial forces. The different nature of these forces and their strong coupling make it difficult to analyze the dynamic aeroelastic response of aircraft structures; although analytical models exist to predict the occurrence of certain aeroelastic phenomena, like flutter [2], the multidisciplinary nature makes wind-tunnel experiments for investigating aeroelastic phenomena on novel aircraft configurations and validating the predictions obtained with such models challenging to perform [3].

A variety of measurement instruments for determination of individual forces are available (e.g., pressure transducers, accelerometers, and load cells), but their coordinated use results in complex and expensive experimental setups. Additionally, installed sensors are invasive to the experimental model, locally changing its shape and/or mass, while providing only discrete information, typically with a relatively low spatial resolution. As a result, experimental reference data from wind-tunnel measurements that can be used for the comparison with theoretical results and for calibrating computational models are typically limited to only a few quantities that are relatively

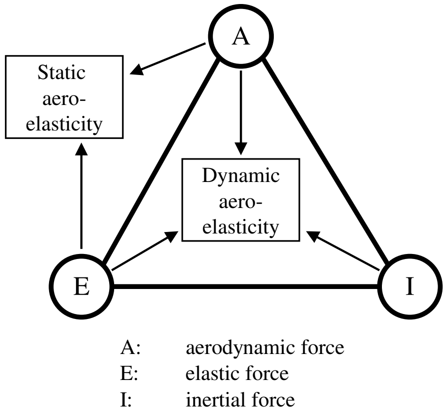

Fig. 1 Illustration of Collar's triangle of forces.

easy to obtain, such as wingtip deflection or frequency of dynamic motion [4].

Modern optical measurement techniques, such as particle image velocimetry/particle tracking velocimetry (PIV/PTV; [5]) for aerodynamics and digital image correlation (DIC; [6]) for structural dynamics, provide noninvasive field measurements, and hence overcome many of the particular limitations associated with the use of installed sensors. The potential of the combined use of these techniques in aeroelasticity experiments is demonstrated in [7], where PIV and DIC were used to simultaneously determine the deformation of a flexible wing and the resulting unsteady position of the wingtip vortex. Similarly, the deformation and aerodynamic loads on a flexible plate were investigated in [8] using DIC and PIV, respectively. These existing studies indicate the capabilities of optical measurement techniques for the nonintrusive characterization of aeroelastic phenomena, but they do not overcome the complication of the coordinated use of several measurement and data processing systems, which would be a requirement for simple and fast production of aeroelastic reference data. This problem was approached for example in [9], where the aerodynamic force in terms of the surface pressure and the deformation of a flexible wing in transonic flow was determined in an integrated approach from pressure-sensitive paint images by using fiducial markers placed on the wing in a photogrammetric approach. However, although this approach facilitates the combined measurement of the aerodynamic and structural behavior with only one optical data acquisition system, it requires two separate system calibrations and data processing methods to obtain these measurements.

The current study proposes the use of PTV to determine all three forces in Collar's triangle with an integrated nonintrusive measurement approach, using only one measurement system that requires minimal instrumentation of the experimental model. The experimental model that is investigated in this study is a flexible wing that is subjected to steady and unsteady periodic inflow conditions. The unsteady periodic inflow is produced with a gust generator that performs a continuous sinusoidal motion upstream of the flexible wing. Optical measurements of the unsteady flowfield and the structural motion are performed in an integrated manner, using the same PTV data acquisition and processing system. Particle tracking velocimetry via the Lagrangian particle tracking algorithm Shake-the-Box [10] using helium-filled soap bubbles (HFSBs) as flow tracers [11] is a technique that is suitable for the measurement of large-scale unsteady flowfields [12–14] and can also be used to perform photogrammetric tracking of fiducial markers on moving objects in the flow [15]. After the PTV measurements of the flow and the structural motion are obtained, physical models need to be applied to determine the unsteady interaction of the forces of different nature on the wing. The identification of suitable procedures to determine the loads based on experimental measurements of the flow velocity and the structural deformation by using physical models is the subject of ongoing research; see, e.g., [16–18], respectively. In this study, relatively simple physical models are used to demonstrate the experimental determination of the forces comprising Collar's triangle for the investigated static and dynamic aeroelastic test cases.

II. Physical Models for the Determination of the Forces

A. Determination of the Aerodynamic Force

The component of the aerodynamic force that predominantly determines the aeroelastic response of a flexible wing is the normal force, which acts perpendicular to the airfoil chord. For small values of the angle of attack α, the drag force is considerably smaller than the lift force, and furthermore $\cos\alpha \approx 1$; see Fig. 2.

As a consequence, the lift force, which acts perpendicular to the direction of the undisturbed inflow x, and the normal force can be treated as equivalent, while the drag force is not further taken into account in this study. The lift per unit span L' of a thin airfoil in steady flow can be determined from the Kutta–Joukowski theorem, based on the assumption of inviscid, incompressible, and irrotational flow [19]:

$$L' = \rho U_\infty \Gamma_b \tag{1}$$

The circulation bound to the airfoil Γ_b can be obtained from a measured flow velocity field $\boldsymbol{u}$ with a line integral over a closed path C around the airfoil:

$$\Gamma_b = -\oint_C \boldsymbol{u} \cdot \mathrm{d}\boldsymbol{s} \tag{2}$$

Although the Kutta–Joukowski theorem was originally derived for steady and irrotational flow, previous studies have observed that it is well suited to determine the lift force from experimental measurements also in flow conditions in which relatively small regions of the flow are rotational due to viscous boundary-layer effects [20,21]. As long as no large flow separation occurs in the measured flowfields, it can therefore be expected that the Kutta–Joukowski theorem is a suitable approach to determine the lift force for steady inflow conditions.

In unsteady inflow conditions, the flow acceleration effects on the unsteady lift have to be considered in addition to the quasi-steady lift due to the circulation that is given by Eq. (1). Following the unsteady thin airfoil theory [22], the unsteady lift $L'(t)$ on a thin airfoil is given as

$$L'(t) = \rho U_\infty \Gamma_b(t) + \rho \int_0^c \left(\frac{\partial}{\partial t} \int_0^x \gamma(\tilde{x}, t)\,\mathrm{d}\tilde{x} \right) \mathrm{d}x \tag{3}$$

The evaluation of the unsteady flow acceleration term, given as the second term in Eq. (3), requires knowledge of the temporal behavior of the distribution of the strength of the bound vortex sheet γ along the camber line that represents the airfoil in the unsteady potential flow model. This expression can be simplified by using Stokes's theorem to replace the integral of the bound vortex sheet with the partial bound circulation Γ_p along the chord:

$$L'(t) = \rho U_\infty \Gamma_b(t) + \rho \int_0^c \left(\frac{\partial}{\partial t} \Gamma_p(x, t) \right) \mathrm{d}x \tag{4}$$

The partial bound circulation along the chord $\Gamma_p(x, t)$ is obtained similarly to the overall bound circulation $\Gamma_b(t)$ by line integrals of the

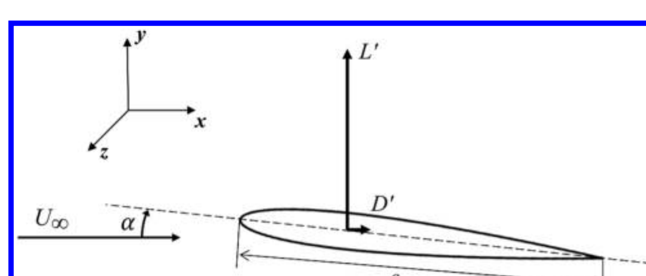

Fig. 2 Sketch of an airfoil with forces and coordinate system.

measured flow velocity. The value of Γ_p at a given chord position x_i is obtained by performing a line integral of the velocity along a contour that encloses the chord of the wing from the leading edge until x_i, at which point the line integration path begins and ends on the airfoil surface.

B. Determination of the Inertial Force

The dominant motion degree of freedom of the considered aeroelastic interaction is the out-of-plane deflection w in the y direction perpendicular to the chord line of the flexible wing. For the purpose of this demonstration study, a simplified 1-D model of the wing with a single coordinate z is considered to perform the characterization of the dominant aspect of the aeroelastic interaction, while the other motion degrees of freedom are not taken into account.

The out-of-plane inertial force per unit span I' on the wing can be determined as the product of mass density and out-of-plane acceleration along the span:

$$I'(z,t) = -\mu(z)\ddot{w}(z,t) \tag{5}$$

where $\mu(z)$ is the mass per unit span, and $\ddot{w}$ is the second temporal derivative of the out-of-plane wing deflection. In the case of steady flow around the wing, $\ddot{w} = 0$ and thus $I'(z) = 0$. In the case of unsteady periodic inflow, such as the inflow produced by the sinusoidal operation of the gust generator at a frequency of ω_g in this study, as described in Sec. III, it can be assumed that the resulting aerodynamic loading on the wing is also sinusoidal. When the structural response of the wing is linear, it follows that the steady-state dynamic response of the wing is sinusoidal as well, with the same frequency as the excitation ω_g. Hence, the steady-state dynamic response of the wing can be written as

$$w(z,t) = w_0(z) + w_a(z)e^{(i\omega_g t+\varphi)} \tag{6}$$

where $w_0(z)$ is the mean deflection, which is identical to the wing deflection in response to the steady inflow, and $w_a(z)$ is the steady-state dynamic deflection amplitude. The second temporal derivative of Eq. (6) is then

$$\ddot{w}(z,t) = -\omega_g^2 w_a(z)e^{(i\omega_g t+\varphi)} \tag{7}$$

The inertial load $I'(z)$, as given in Eq. (5), is determined in this study by performing a sinusoidal curve fitting to the PTV-based marker displacements from their respective mean values over the period, to determine $w_a(z)$ as well as the phase lag φ, and thus $\ddot{w}(z)$ according to Eq. (7).

C. Determination of the Elastic Force

For the determination of the elastic force as a part of the aeroelastic characterization in this study, only the shear force acting normal to the wing surface is considered. The flexible wing is therefore modeled as an Euler–Bernoulli beam along the wingspan, where the analysis is restricted to the bending deflection $w(z)$ across the span. The wing is clamped at the root so that $w(z=0) = 0$ and $w'(z=0) = 0$ are used as Dirichlet boundary conditions in the beam model. The Euler–Bernoulli equation that establishes a relation between the deflection and the external load on the wing $q(z)$ in the static case is

$$\frac{d^2}{dz^2}\left(\mathrm{EI}(z)\frac{d^2w(z)}{dz^2}\right) = q(z) \tag{8}$$

while the shear force $Q(z)$ and the bending moment $M(z)$ in the beam are

$$Q(z) = -\frac{d}{dz}\left(\mathrm{EI}(z)\frac{d^2w(z)}{dz^2}\right) \tag{9}$$

$$M(z) = -\mathrm{EI}(z)\frac{d^2w(z)}{dz^2} \tag{10}$$

The effective flexural rigidity $\mathrm{EI}(z)$ is assumed to be known for this study, by extracting the values from the Timoshenko beam model of the same wing that is used in [23], where it was observed to yield results that are in good agreement with experimental data obtained from wind-tunnel tests. The effective flexural rigidity varies along the span so that a finite element beam model is used to solve Eq. (8). In the static case, the governing equation of the finite element beam model is

$$\boldsymbol{K}\boldsymbol{\xi} = \boldsymbol{D}\boldsymbol{f} \tag{11}$$

where $\boldsymbol{K}$ is the stiffness matrix, $\boldsymbol{D}$ is the loading matrix, $\boldsymbol{f}$ is the external force vector, and the vector $\boldsymbol{\xi}$ contains the values of the nodal degrees of freedom, which are the deflections and the rotations. The continuous beam deflection $w(z)$ is calculated from the discrete values of the degrees of freedom by using Hermite splines, and $\boldsymbol{f}$ is determined by sampling the distribution of the external load $q(z)$ at the nodes of the finite element model. More details on the finite element method that was used in this study can be found in sec. 3.5.3 in [24].

In this study, the presence of measurement noise impedes the direct determination of the elastic force with Eq. (11) from the optical displacement measurements. Instead, the elastic force is determined by performing an optimization of the external load $q(z)$, so that the corresponding beam deflection $w(z)$ best matches the measurements. Because of the relatively small spanwise region where measurements are available in this particular study, it is necessary to make an assumption of the behavior of the external load across the span to achieve meaningful results with this approach. In this study, it is assumed that the external load on the beam is constant across the span with $q(z) = q_0$, so that q_0 is the only optimization variable. This means that the lift reduction effects on the wing loading due to downwash near the wingtip are not taken into account, which can be justified with the relatively large aspect ratio of the wing.

Following the optimization procedure for q_0 in the static case, the shear force and the bending moment in the beam are determined with Eqs. (9) and (10), which can be solved analytically in the case of a given constant external load in the static case, when considering the Neumann boundary conditions $Q(z=s) = 0$ and $M(z=s) = 0$ at the free end:

$$Q(z) = -\int q_0 \mathrm{d}z = -q_0(z-s) \tag{12}$$

$$M(z) = \int Q(z)\mathrm{d}z = -\frac{q_0}{2}(z^2 - 2zs + s^2) \tag{13}$$

In the case that the wing is moving dynamically, the governing equation for the Euler–Bernoulli beam is enhanced with the inertia term:

$$\frac{\partial^2}{\partial z^2}\left(\mathrm{EI}(z)\frac{\partial^2 w(z,t)}{\partial z^2}\right) + \mu(z)\frac{\partial^2 w(z,t)}{\partial t^2} = q(z,t) \tag{14}$$

and equivalently for the finite element model of the beam

$$\boldsymbol{K}\xi(t) + \boldsymbol{M}\ddot{\xi}(t) = \boldsymbol{D}\boldsymbol{f}(t) \tag{15}$$

where $\boldsymbol{M}$ is the mass matrix, as determined from the mass distribution properties of the experimental model.

If the assumed loading is given by $\boldsymbol{f}(t) = \boldsymbol{f}_0 + \boldsymbol{f}_a e^{i\omega_g t+\varphi}$, for a linear system the response is the superposition of the static and steady-state dynamic response $\boldsymbol{\xi}(t) = \boldsymbol{\xi}_0 + \boldsymbol{\xi}_a e^{i\omega_g t+\varphi}$. The relation between the dynamic wing response amplitude $\boldsymbol{\xi}_a$ and the external load amplitude $\boldsymbol{f}_a$ does not depend on the time explicitly:

$$(\boldsymbol{K} - \omega_g^2\boldsymbol{M})\boldsymbol{\xi}_a = \boldsymbol{D}\boldsymbol{f}_a \tag{16}$$

Similar to the steady case, Eq. (16) is used in this study to optimize for the amplitude q_a of a sinusoidal, spanwise-constant external load by fitting the finite element model beam deflection due to a given load to the wing deformation amplitude that is obtained from the experimental measurements. In this case, it is not trivial to derive analytical expressions for the shear force and the bending moment in the beam so that in the test case with unsteady inflow, these quantities are computed from the deflection with Eqs. (9) and (10).

III. Experimental Setup

A. Wind-Tunnel Setup

The experiments were conducted in the Open Jet Facility of Delft University of Technology, which is a closed-loop open-test-section wind tunnel with an octagonal exit of $2.85\times2.85\,\mathrm{m}^2$. The wind tunnel is powered by a 500 kW electric motor, which drives a fan that can provide freestream velocities of up to $35\,\mathrm{m\cdot s^{-1}}$ in the test section. In this study, the freestream velocity was set to $U_\infty = 14\,\mathrm{m\cdot s^{-1}}$, which corresponds to a Reynolds number of around 2.3×10^5 based on the chord of the flexible wing. The wind-tunnel setup is shown in Fig. 3.

For this study, a gust generator is mounted at the wind-tunnel nozzle exit, which can generate various types of unsteady inflow conditions to the model in the test section [25]. The following two experimental test cases are considered in this study: one test case with steady inflow, where the gust generator is not operated, and a second test case with periodic unsteady inflow, where the gust generator is operated continuously with a sinusoidal variation of the gust vane angle β according to $\beta(t) = 5\ \deg\times\sin(\omega_g t)$, where $\omega_g = 2\pi f_g$ is the angular frequency of the gust vane motion. The selected frequency of $f_g = 2$ Hz corresponds to a reduced frequency of $k = (f_g \pi c)/U_\infty = 0.11$ and is expected to cause appreciable unsteady aerodynamic effects on the flexible wing model [26].

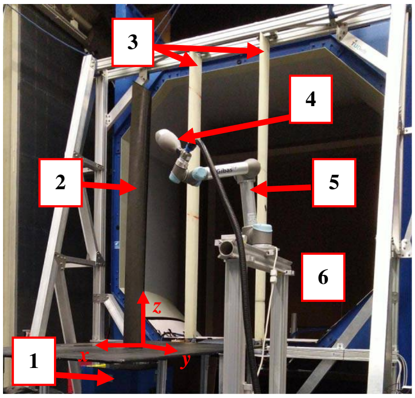

Fig. 3 Photograph of the wind-tunnel setup: 1, six-component balance; 2, flexible wing model; 3, gust generator; 4, coaxial volumetric velocimeter; 5, robotic arm; and 6, helium-filled soap bubbles seeding generator.

To perform the PTV measurements of the flow, the freestream is seeded with HFSB flow tracers with a diameter of about 0.5 mm. The HFSBs are generated by a seeding generator that consists of 200 bubble-producing nozzles over an area of $0.5\times1\ \mathrm{m}^2$. The working principle of the bubble-producing nozzles is described in [27]. To improve the seeding concentration and to minimize the influence of the seeding generator on the turbulence intensity of the freestream, the seeding generator is placed in the settling chamber of the wind tunnel, upstream of the wind-tunnel nozzle, and is therefore not visible in Fig. 3.

B. Flexible Wing Model

The experimental model is a rectangular wing with a chord length of $c = 0.25$ m, a span width of $s = 1.75$ m, and a NACA 0010 profile that is oriented at a geometric angle of attack of $\alpha = 5$ deg with respect to the freestream. The wing was constructed in-house out of carbon-fiber-reinforced epoxy unidirectional tailored laminates. Its inner structure is formed by 2 spars and 13 ribs, and the outer skin is divided into three spanwise regions of equal length with different laminate thickness and stiffness properties. The laminate properties were optimized to minimize the structural weight of the wing and to maximize the wing compliance. The design and manufacturing procedure of the flexible wing model is described in detail in [23]. To enable the PTV measurements of the wing displacement, a rectangular grid of white circular markers is spray painted on the surface of the wing model using a laser-cut template. The markers have a diameter of 1.5 mm and the grid spacing is 30 mm. The marker grid on the wing is detailed in Fig. 4.

The flexible wing model is clamped to a six-component balance using an aluminum plug, which is glued to the bottom of the wing. The mass of the wing without the aluminum plug is 1.44 kg. The dynamic motion amplitude of the flexible wing in response to the unsteady inflow generated by the gust vanes is increased by inserting a wingtip mass of 0.40 kg, which reduces the frequency of the first bending mode of the wing from 5.4 to 3.3 Hz, which is close to the excitation frequency f_g, thus generating larger dynamic wing deformations. With the experimental parameters employed in this study, the maximum wingtip deflection is around 40 mm, corresponding to around 2% of the span.

The measurements of the six-component balance on which the wing is mounted are used for validation purposes of the loads at the root of the wing, as determined with the beam model based on the PTV measurements. Additionally, the wing model is equipped with a Luna HD6 fiber optic strain sensor that is mounted at midchord on the inside

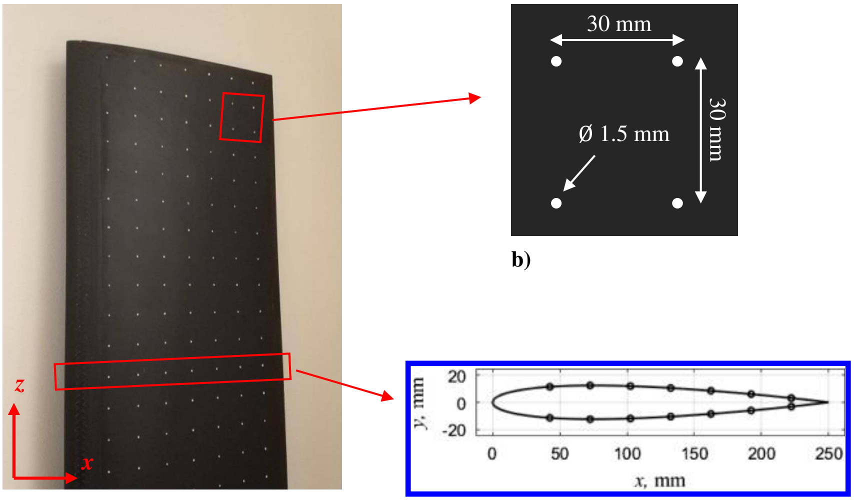

Fig. 4 Structural markers grid, a) photograph of the wing, b) grid dimensions, c) chordwise distribution.

of the pressure side of the wing, from the root until $z = 1.65$ m or 94% of the span. The strain measurements from the optical fiber installed in the wing are obtained with a Luna ODiSI data acquisition system and are used for validating the strains that are obtained from fitting the Euler–Bernoulli beam model to the PTV marker measurements.

C. Particle Tracking Velocimetry System

The primary measurement component that is used for the PTV measurements is a LaVision MiniShaker Aero coaxial volumetric velocimetry (CVV) probe [28]. The CVV features four complementary metal oxide semiconductor cameras for image acquisition that are mounted in a compact housing (dimensions $130 \times 90 \times 80$ mm^3) together with the coaxial illumination component, which consists of an optical fiber with a diverging lens at the end to illuminate the particles in the field of view of the cameras. As illumination source, a Quantronix Darwin-Duo Nd:YLF laser (25 mJ pulse energy at 1 kHz; wavelength of 527 nm) is connected to the other end of the optical fiber. The compactness of the CVV probe allows it to be mounted on a Universal Robots UR5 robotic arm, which has six motion degrees of freedom and a maximum reach of 0.85 m. The controlled positioning of the CVV in space with the robotic arm enables the measurement of several adjacent volumes without performing repeated calibrations of the CVV. Furthermore, it also allows a simple merging of the measurement volumes during postprocessing, which facilitates the measurement of flowfields around objects on a cubic meter scale [29].

The optical measurements of the flow and the structure are conducted with the maximum acquisition frequency of the CVV of $f_s =$ 821 Hz and with the maximum camera sensor size for that acquisition frequency, which is 704×540 pixel. Six different positions of the CVV with respect to the wing are used to obtain the flow measurements around the investigated wing section, with three different chordwise positions of the CVV on the pressure and suction sides, respectively. To achieve this, the optical measurement setup is installed successively on both sides of the wing. The combined size of the measurement volumes with this procedure is around 15 liters. For the case of steady inflow, 15,000 images are acquired per individual measurement volume. For the case of dynamic inflow, 98,520 images are acquired over 240 motion periods per measurement volume.

IV. Integrated Measurement Approach

A. Data Processing

The complete data processing procedure that is followed in this study is illustrated in Fig. 5. The processing procedure for the acquired data begins with the separation of the flow tracers from the structural markers in the acquired images. This step improves the performance of the PTV algorithm Shake-the-Box because the appearance of the structural markers and the flow tracers in the images is not identical. After the separation is performed, a nonuniform optical transfer function [30] can be generated for the structural markers and the flow tracers separately. The removal of the structural information from the integrated measurement images is achieved with a temporal high-pass filter [31], exploiting the different timescales of the structural motion and that of the flow. In principle, reverse operation can be applied to obtain the image data of the structural markers without the flow tracer information using a temporal low-pass filter, as it was done in [15]; however, in this study, this step is not directly necessary because the observed phenomena are either steady or periodic, and thus repeatable over time. This means that the isolated structural marker information can be simply obtained by acquiring images without operating the HFSB seeding generator, as shown in Fig. 6. This approach is advantageous because it allows the modification of the camera sensor size to the maximum of $704 \times$ 636 pixel, which permits the simultaneous measurement of all markers along the chord with just one acquisition at a sampling frequency $f_s = 500$ Hz. These additional measurements of only the structural motion are conducted only on the pressure side of the wing. It is presumed that the measurements from the other side of the wing do not provide any additional information, given the relatively low

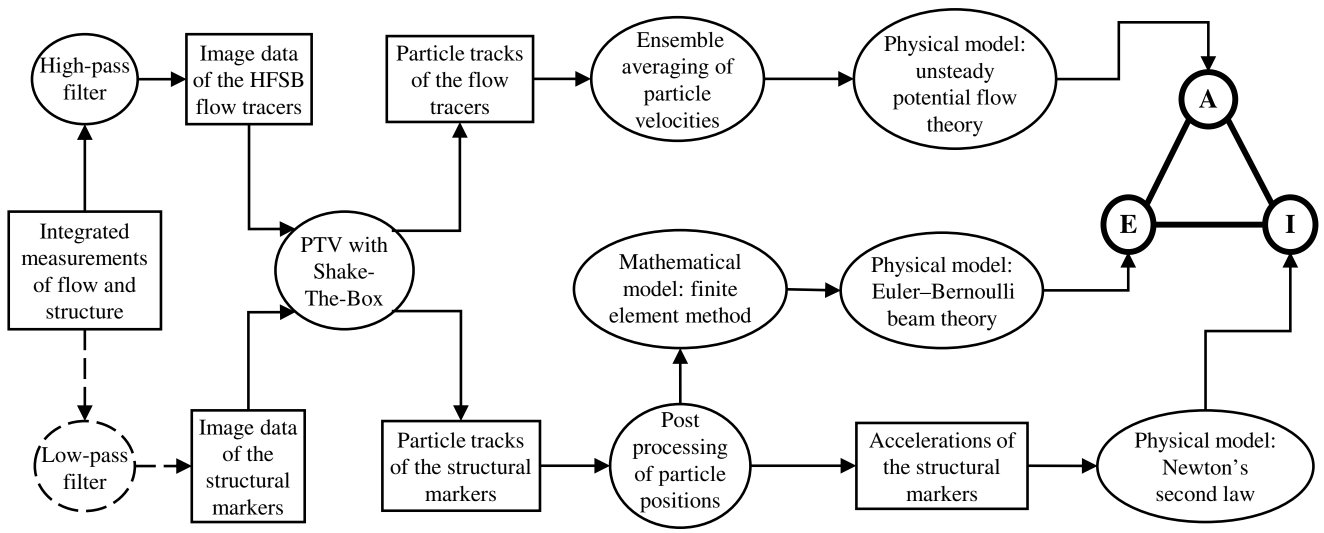

Fig. 5 Data processing procedure for the aerodynamic and structural measurements.

Fig. 6 PTV image data processing: a) integrated measurement, b) flow tracers, c) structural markers.

density of the marker grid, the small deformation of the investigated spanwise region, and the relatively low complexity of the structural model that is used to analyze these measurements, which does not consider shear deformations.

After separating the flow and structural information, the next step is to apply the particle tracking algorithm. The method used for obtaining the PTV measurements consists of the following three steps that are performed separately for the flow and the structure: first, a volume self-calibration [32] is performed, then an optical transfer function is generated, and afterward the Shake-the-Box algorithm is applied. Results are obtained in terms of individual particle tracks, with position, velocity, and acceleration of each particle over time, for both the structural markers and the flow tracers in separate files. Once the track data of the flow tracers are obtained, the velocities of the flow tracer tracks are ensemble averaged to a 3-D Cartesian grid with a spacing of 2.5 mm, using a top-hat filter approach with cubic bins of $10 \times 10 \times 10$ mm^3, as described in [33]. For the measurements obtained in the case of steady inflow, the particle tracks obtained from all acquired images are combined in the ensemble-averaging procedure. For the measurements with dynamic periodic inflow, the particle tracks are ensemble averaged in a phase-averaged sense based on the recorded signal of the gust generator motion, where the particle tracks are assembled in 100 temporal bins, each spanning 1% of the gust excitation period $T = f_g^{-1}$.

The particle tracks of the structural markers are processed in two different postprocessing procedures for the cases of steady and unsteady inflows, respectively. In the case of steady inflow, the marker track positions within a radius of 10 mm are averaged to obtain the mean position of the observed grid of markers in space. This step is necessary to overcome the relatively large random error in the position measurement of the markers, which has a typical value on the order of 1 mm [15]. The same procedure is then repeated for a reference measurement of the marker positions without wind-tunnel operation. Subsequently, the difference between the two grids is calculated to obtain the static deflection of the wing. The physical model is then fitted to these results to determine the elastic forces, as explained in Sec. II. For the analysis of the test case with unsteady inflow, only the amplitude of the deflection around the mean is required in the physical model for the determination of the inertial force and the elastic force, as the considered linear elastic theory suggests that the mean value of the deflection is given by the result for the case of steady inflow. The marker position measurements over time are phase averaged in 100 temporal bins, which is identical to the processing of the flowfield so that the combination of the model position with the flowfields is coherent. The mean value of these position measurements per marker over the entire period is then subtracted from the phase-averaged positions to obtain the dynamic displacement of the respective marker over the cycle. In both test cases, no significant relation was observed between the chordwise position of the marker and the deflection, indicating negligible twist of the wing, allowing the marker information to be averaged along the chord. This also supports the assumption that measuring on only one side of the wing is sufficient because the cross section of the wing is not deforming. As shown in Fig. 5, the physical model for the determination of the elastic force requires the position measurements as input, while the determination of the inertial force requires measurements of the acceleration, which are computed from a sinusoidal fit to the phase-averaged position measurements in time.

B. Closure of Collar's Triangle

After the aerodynamic, inertial, and elastic forces are determined with the three described methods from the integrated measurements, the results can be combined in an internal validation procedure, where the physical agreement of the three different models with each other can be quantified. To visualize the different forces acting on the wing, a free-body diagram of a wing section between the spanwise positions z_1 and z_2 is illustrated in the free-body diagram in Fig. 7.

The equilibrium of the forces acting on the wing section in the direction of the deflection w in Fig. 7 is as follows:

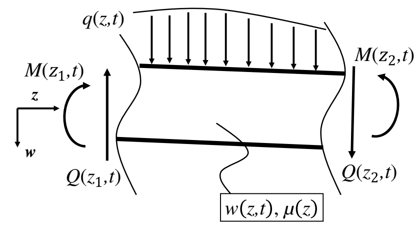

Fig. 7 Free-body diagram of a wing section.

$$\int_{z_1}^{z_2} q(z,t)\mathrm{d}z - Q(z_1,t) + Q(z_2,t) - \int_{z_1}^{z_2} \mu(z)\ddot{w}(z,t)\mathrm{d}z = 0 \quad (17)$$

The three forces in Collar's triangle that are involved in a dynamic aeroelastic interaction (aerodynamic force A, elastic force E, and inertial force I) can be recognized in Eq. (17):

$$A = \int_{z_1}^{z_2} L'(z,t)\mathrm{d}z = \int_{z_1}^{z_2} q(z,t)\mathrm{d}z \quad (18)$$

$$E = -Q(z_1,t) + Q(z_2,t) \quad (19)$$

$$I = \int_{z_1}^{z_2} I'(z,t)\mathrm{d}z = -\int_{z_1}^{z_2} \mu(z)\ddot{w}(z,t)\mathrm{d}z \quad (20)$$

which means that the dynamic equilibrium of forces, which is given by Eq. (17), can be stated as $A + E + I = 0$ for the wing segment that is investigated in this study. This requirement is verified in this study by calculating a measurement residual, defined as $\delta = A + E + I$, which is then used to quantify the error of the considered approach.

V. Results

A. Steady Inflow

For the test case with steady inflow, the aerodynamic force is determined from the measured flow velocity field and the elastic force is determined from the marker position measurements, while the inertial force is zero. The reaction force and moment at the root in the finite element model, which is used to determine the elastic force in the investigated wing section, can be validated against the balance measurements. The strain that results from the application of the determined external force to the beam model is compared with the optical strain fiber measurements. The elastic force on the segment is in equilibrium with the aerodynamic force in the absence of inertial forces so that a comparison of the two forces is performed and the residual of the considered approach is computed.

1. Elastic Force

The result for the deflection $w(z)$ of the finite element beam model as fitted to the PTV marker displacement measurements is shown in Fig. 8. The standard deviation σ in displacement for the seven chordwise markers that were used to produce one average displacement per spanwise position has values in the range of 0.28 mm $< \sigma <$ 0.61 mm. After updating the value of the external load q_0 with an optimization procedure to achieve the best match of the beam model with the displacement measurements, as described in Sec. II.C, the agreement between the beam deflection and the chordwise-averaged marker displacement is very good, with an root-mean-squared (rms) value of the difference between the measurement and model of 0.10 mm.

The result for the deflected shape can be validated against the measurements from the optical strain fiber that is installed inside the skin on the pressure side of the wing. For this purpose, the strains according to the beam model are computed from the deflection line by using the equation for the strain of an Euler–Bernoulli beam:

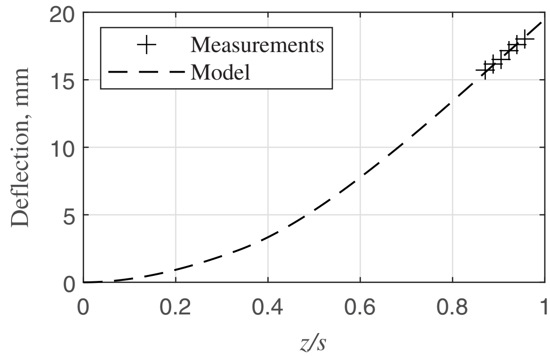

Fig. 8 Finite element beam model fitted to the static PTV measurements.

$$\varepsilon = -\frac{d^2 w}{dz^2} h_1 \tag{21}$$

where $h_1 = 11$ mm is the distance of the optic fiber from the elastic axis of the beam, which is assumed to be at the chord line of the wing. The comparison between the strain measurement and the model strain is shown in Fig. 9. The cross-sectional stiffness properties of the wing change at $z/s = 1/3$ and $z/s = 2/3$, as described in [23], which results in a discontinuity of the strain in the beam model at these locations. In contrast, the strain fiber is installed on the inside of the surface at the pressure side of the wing, where the stiffness properties only change at $z/s = 1/3$; therefore, the strain that is measured with the optical fiber is only discontinuous at that location and not at $z/s = 2/3$. Apart from this difference, the agreement between the model and the measurement is very good.

The result for the external load q_0 can be used to calculate the shear force and the bending moment at the root of the flexible wing with Eqs. (12) and (13). The value for the shear force can be directly compared to the force measurement of the balance, as shown in Table 1, where the mean value and one standard deviation of the balance measurements are given. For the comparison of the bending

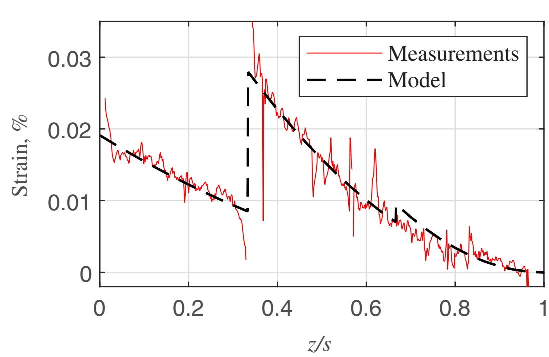

Fig. 9 Comparison of the strain between the finite element beam model and the optic fiber measurements.

Table 1 Comparison of model reaction forces at the root clamp with balance measurements

Quantity	Balance measurement	Finite element model	Relative error, %
Root shear force $Q(z=0)$	-15.82 ± 1.73 N	-17.34 N	9.64
Root bending moment $M(z=0)$	-13.20 ± 0.84 N $\cdot$ m	-15.18 N $\cdot$ m	14.94
CP	$0.477 \times s$	$0.5 \times s$	4.84

moment with the balance measurement, the distance from the center of the balance to the root of the wing $h_2 = 334$ mm has to be considered. The root bending moment from the balance is determined from the balance measurements of the shear force and the moment under the assumption that no external bending moment is applied on the wing:

$$M(z=0)_{\text{balance}} = M_{\text{balance}} - Q_{\text{balance}} \times h_2 \tag{22}$$

A modeling assumption that is considered as a source of the observed differences in shear force and bending moment in Table 1 is that of a constant external load along the span. The validity of this assumption can be assessed by calculating the spanwise center of pressure (CP; m):

$$\text{CP} = \frac{M(z=0)}{Q(z=0)} \tag{23}$$

The balance measurements in Table 1 reveal that CP is located slightly further inward on the wingspan than in the assumed case of a spanwise-constant load, where CP is located at midspan, differing by less than 5%, which indicates that the constant-load assumption is not the dominant source of error in the considered approach.

2. *Aerodynamic Force*

A section of the ensemble-averaged flowfield, located at $z/s = 0.90$, is shown in Fig. 10, together with the position of the wing section that is determined from the marker position measurements. Furthermore, the black rectangle in the plot indicates an exemplary rectangular integration contour for the calculation of the circulation around the airfoil. The shown integration contour is positioned such that a minimum distance of 25 mm, which is equivalent to 0.1 chord lengths, to the surface of the wing is observed in all directions.

The circulation measurement that is obtained from the flowfield is used to calculate the section lift with the Kutta–Joukowski theorem [Eq. (1)], as shown for all spanwise sections, where flow measurements were conducted in Fig. 11. In theory, the result for the lift is independent of the choice of the integration contour around the airfoil, which is used to determine the circulation. To reduce the sensitivity of the lift to the random error in the flow velocity measurements, the lift is therefore computed as the average of the lift values that are obtained when

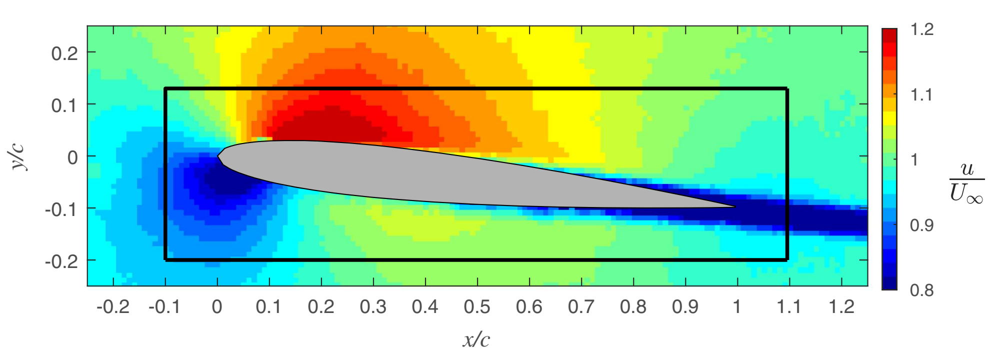

Fig. 10 Flowfield, airfoil position, and circulation integration contour at $z/s = 0.90$.

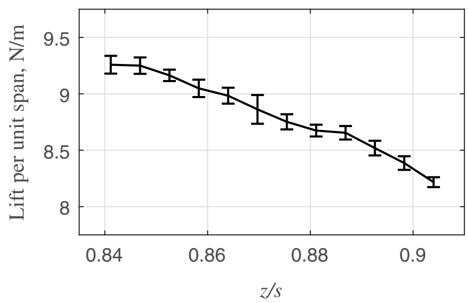

Fig. 11 Lift from the Kutta–Joukowski theorem in the investigated wing section.

varying the distance of the rectangular circulation integration contour to the wing surface from 0.05 to 0.2 chord lengths in $0.025c$ increments, for each spanwise position. The spanwise average of the standard deviation of the circulation obtained with the different integration contours is $\sigma\Gamma_b = 0.004\ \mathrm{m^2/s}$, which is less than 1% of the spanwise average of the circulation, $\Gamma_b = 0.523\ \mathrm{m^2/s}$. The variations in the lift that result from using the different circulation integration contours were used to indicate the lift uncertainty in Fig. 11, where the error bars represent one standard deviation.

The aerodynamic force that is exerted on the investigated wing segment can be compared with the elastic force that is determined from the marker measurements with the finite element model. When considering the wing segment between $z_1/s = 0.85$ and $z_2/s = 0.9$, the aerodynamic force on the segment can be calculated from the lift distribution shown in Fig. 11 with a trapezoidal integration:

$$A = \int_{z_1}^{z_2} L'(z)\mathrm{d}z = 0.7691\,\mathrm{N} \tag{24}$$

while the elastic force on the segment with $q_0 = 9.91\ \mathrm{N \cdot m^{-1}}$ is

$$E = -Q(z_1) + Q(z_2) = q_0(z_1 - z_2) = -0.8672\,\mathrm{N} \tag{25}$$

According to the equilibrium of forces in Collar's triangle for the case of static aeroelasticity, the two forces A and E on the segment are equivalent in the absence of structural motion, and hence inertial forces, which leads to the quantification of the observed measurement residual as $\delta = A + E = -0.0981$ N. The value for the measurement residual is used to calculate a relative error of the considered approach for the case of steady inflow. To provide a reference force, the balance measurement of the shear force at the root is scaled by the fraction of the investigated wing section, which is $(z_2 - z_1)/s = 0.05$. This yields a reference force value of −0.791N with a corresponding relative residual of $\varepsilon = 12.41\%$ for the case of steady inflow, which is accredited to the difference between the elastic properties of the wing and the beam model, and to the drop in lift toward the tip due to downwash effects, which is observed in Fig. 11, but not considered in the structural model.

B. Unsteady Periodic Inflow

For the dynamic aeroelastic test case with unsteady periodic inflow, all three forces in Collar's triangle have to be considered. The analysis of the dynamic structural motion is based on the assumption of a linear elastic response to a sinusoidal external forcing. The result of a sinusoidal fit to the marker position measurements can be used to validate this assumption and to determine the acceleration, and hence the inertial force on the investigated wing segment. The amplitude of the marker displacement measurements is used to determine the amplitude of the dynamic elastic force with the finite element model. The unsteady aerodynamic force is determined from the measured flowfields and is subsequently compared to the inertial and elastic forces according to the equilibrium of forces in Collar's triangle.

1. *Inertial Force*

For the determination of the inertial force, the acceleration is determined from the phase- and chordwise-averaged marker displacement measurements by fitting a sinusoidal curve according to Eq. (6) through the measurements. The result is shown in Fig. 12, for the spanwise position at $z/s = 0.90$. The sinusoidal fit is seen to be a very good representation of the actual measurements, with an rms of the difference between the fit and the measurements of around 0.2 mm, which is less than the typical standard deviation of the measurements during the phase and chordwise averaging of the marker measurements, which is around 0.3 mm.

The discrete amplitude measurements that are obtained at the spanwise positions of the fiducial markers are used to estimate the continuous behavior of the wing motion in the investigated region. Because the measurements are performed near the tip, it can be assumed that the wing deformations in the sense of spanwise curvature are small and the measured amplitudes can be fitted with a linear curve, which is confirmed in Fig. 13.

With the obtained linear relation between the spanwise position on the investigated wing segment and the amplitudes of the sinusoidal fit according to Eq. (6), it is possible to determine the inertial forces on the segment between z_1 and z_2 with Eq. (7). Furthermore, the amplitude value of the linear fit at $z/s = 0.875$ is used for the determination of the elastic force in the following.

2. *Elastic Force*

For the determination of the elastic force in the dynamic case, the amplitude of the sinusoidal forcing q_a is determined from the observed wing motion amplitude w_a. For that, the finite element formulation of the dynamic beam bending motion in Eq. (16) is solved in an optimization procedure for q_a that minimizes the difference in displacement amplitude between the model and the measurement, as described in Sec. II.C. With the resulting finite element degrees of freedom $\boldsymbol{\xi}_a$ that are the best fit to the experimental data, the dynamic behavior of the finite element model degrees of freedom is given as $\boldsymbol{\xi}_a e^{i\omega_g t+\varphi}$, where the phase was aligned with the sinusoidal fit of the marker measurements so that $\varphi = 0$.

From this result for $\boldsymbol{\xi}(t)$, the continuous time-dependent deflection $w(z,t)$ is calculated with the Hermite spline interpolation for each time step. Then, the shear force $Q(z,t)$ and bending moment $M(z,t)$

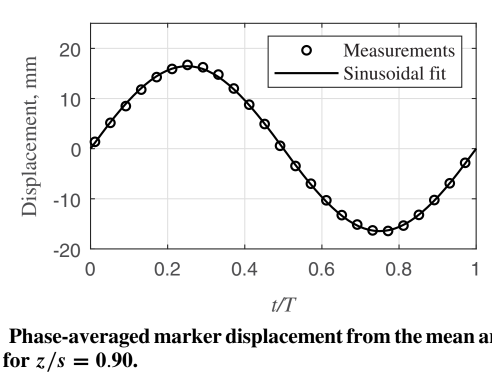

Fig. 12 Phase-averaged marker displacement from the mean and sinusoidal fit for $z/s = 0.90$.

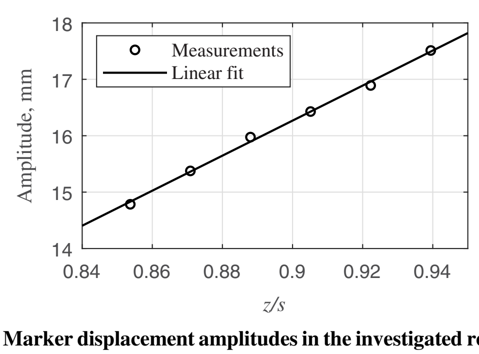

Fig. 13 Marker displacement amplitudes in the investigated region and linear fit.

along the span are obtained with Eqs. (9) and (10) from the deflection by using a second-order-accurate finite difference scheme. With the results of this procedure, the dynamic component of the shear force and the bending moment for comparison with the dynamic component of the balance measurements can be computed over the period. The comparison is shown in Fig. 14, where the mean value has been subtracted from the balance measurements.

The rms value of the difference between the model and the measurement is 1.43 N for the shear force and 1.26 N · m for the bending moment, corresponding to a relative error of 17.10% and 15.01%, respectively, using the rms of the balance measurements as a reference. The phase alignment between the model and the measurement is very good for both the force and the moment, with phase differences of less than 0.5% of the period determined by cross correlating the signals.

3. Aerodynamic Force

The phase-averaged unsteady flowfield and the corresponding wing position as determined from the marker tracks are shown for four phase instants over the period in Fig. 15. The effect of the impinging gusts is evident in the plots, with a visibly enlarged and reduced region of accelerated flow over the suction surface of the wing at $t/T = 0.25$ and $t/T = 0.75$, respectively.

The calculation of the unsteady lift with Eq. (4) requires the determination of the circulation distribution on the airfoil over the entire period. The partial circulation $\Gamma_p(x,t)$ is obtained by performing line integrals of the measured velocity, as defined in Sec. II, for each phase instant. Similar to the test case with steady inflow, the position of the integration path is varied to reduce the effect of the random error in the flow velocity measurements on the result for the circulation. However, in this case, only the positions of the line segments that are upstream, above, and below the airfoil are varied, whereas the downstream segment remains fixed at the particular x location on the airfoil to determine the value of $\Gamma_p(x,t)$ at that specific location. To determine the overall bound circulation around the airfoil $\Gamma_b(t) = \Gamma_p(x = c, t)$, the downstream segment of the integration path also remains fixed just behind the trailing edge of the airfoil, so that the varying circulation that is shed into the wake in the unsteady case following Kelvin's theorem is not affecting the determined result for the bound circulation $\Gamma_b(t)$. The mean value over the period of the standard deviation of the circulation obtained with different integration contours, as described previously, is $\sigma\Gamma_b(t) = 0.024\ \mathrm{m^2/s}$, which is increased by a factor of around 6 with respect to the standard deviation of the circulation that was obtained with a similar procedure for the test case with steady inflow. This increase results from the higher level of random error in the phase-averaged measurements of the unsteady periodic inflow when compared to the steady case, because the number of acquired images is approximately 15 times smaller for a time span of 1% of the period T in the unsteady inflow case than in the case with steady inflow. To reduce the level random error in the measurement, the determined time series of $\Gamma_p(x,t)$ is fitted with a sinusoidal curve for each chordwise position. Furthermore, the partial circulation is averaged across the span in the region z_1 to z_2 so that the average lift per unit span on the investigated wing segment is determined. The result is shown for four different phase instants in Fig. 16.

By using Eq. (1) together with the overall bound circulation around the airfoil $\Gamma_b(t)$, as determined from the unsteady flowfields, the quasi-steady lift is obtained. To determine the unsteady lift, the additional flow acceleration term is computed from the time series of the circulation distribution with Eq. (4). Both lift curves over the

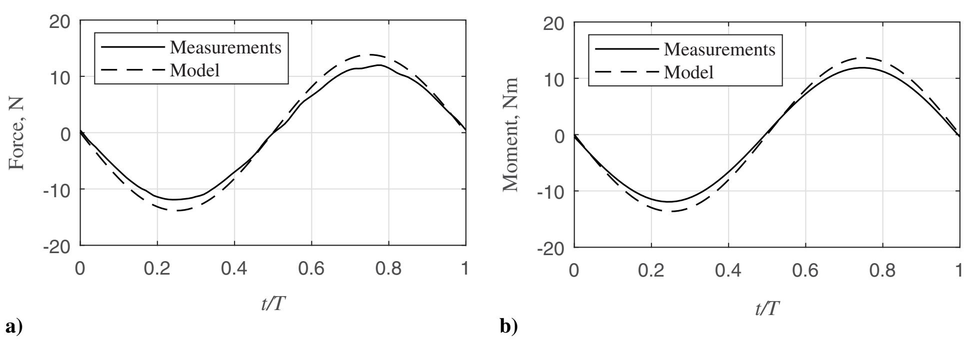

Fig. 14 Dynamic component of the root loads from the finite element model in comparison with the balance measurements, a) root shear force, b) root bending moment.

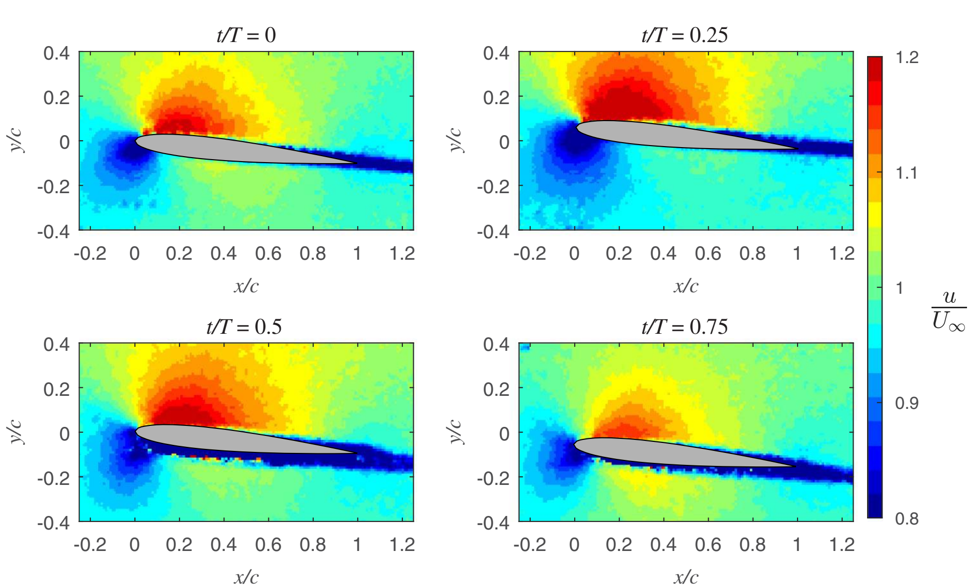

Fig. 15 Flowfield and airfoil position for four different phase instants at $z/s = 0.88$.

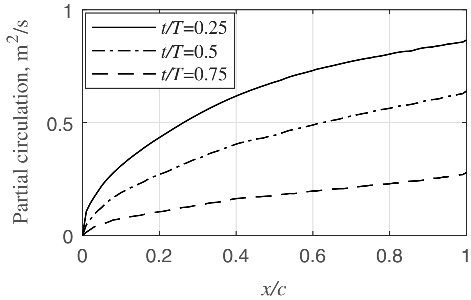

Fig. 16 Partial circulation along the chord for three different phase instants.

period are shown in Fig. 17. The unsteady lift curve as determined from the sinusoidal fit is similar to the quasi-steady lift curve. As a result of including the flow acceleration term in Eq. (4), the amplitude of the unsteady lift is decreased by 0.7% compared to the quasi-steady lift, and the curve is shifted by −2.70% of the period. The lag of the lift with respect to the dynamic motion of the wing is reduced from 3.62% to 0.92% of the period when including the flow acceleration term, which leads the quasi-steady lift in phase.

4. Closure of Collar's Triangle

After the three forces in the dynamic aeroelastic interaction are determined based on the PTV measurements, the results can be compared with each other to validate the physical models based on the equilibrium of forces. The aerodynamic and inertial forces on the segment are determined directly with an integration of the obtained results from z_1 to z_2. For the determination of the elastic force on the segment, the amplitude of the dynamic motion of the finite element degrees of freedom $\boldsymbol{\xi}_a$ is combined with the solution in the case of steady inflow $\boldsymbol{\xi}_0$ to yield the dynamic result $\boldsymbol{\xi}(t) = \boldsymbol{\xi}_0 + \boldsymbol{\xi}_a e^{i\omega_g t + \varphi}$, which is used to calculate the shear forces $Q(z_1, t)$ and $Q(z_2, t)$ with finite differences. The results for the three forces on the investigated wing segment are shown in Fig. 18. Additionally, the value of the residual δ is shown over the period.

The maximum absolute value of δ over the period is 0.158 N at $t/T = 0.23$, which is near the maximum values of the elastic and aerodynamic force magnitudes. The rms value of δ over the period is 0.0964 N, which corresponds to an error of 11.72% of the reference force from the balance, which is the mean value over the period of the measured root shear force, scaled by the fraction of the investigated wing section. This value of the error in the dynamic aeroelastic test case is very similar to the value of the error in the static aeroelastic test case. It can therefore be assumed that the sources of error are the same as in the static case, especially when considering that the result from the static test case has been used to obtain the result for the dynamic shear force. As a consequence, it is noted that the added complexity of the dynamic test case, with considerable unsteady aerodynamic and inertial forces, is suitably accounted for with the applied methods and does not lead to significant additional sources of error.

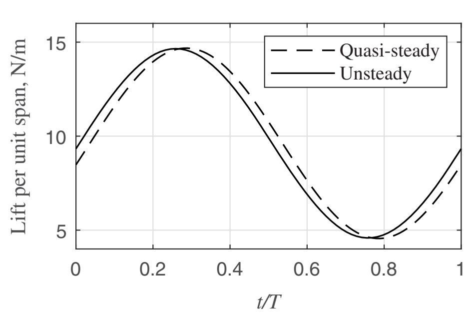

Fig. 17 Quasi-steady and unsteady lift over the period.

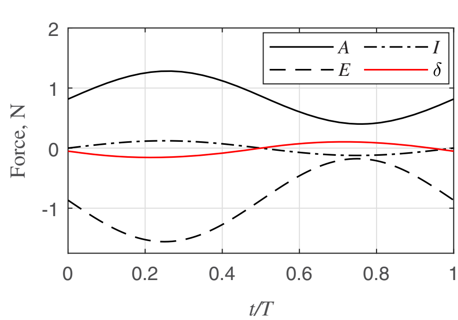

Fig. 18 Three forces in Collar's triangle *A*, *E*, *I* as determined from the PTV measurements and residual δ.

VI. Conclusions

This study demonstrated the possibility to fully characterize the aeroelastic response of a flexible wing in terms of all three force components in Collar's triangle, based on nonintrusive PTV measurements with a single measurement and data processing system. To perform the measurements of the aeroelastic interaction between the flexible wing and the flow, the freestream was seeded with HFSB and the flexible wing model was painted with a grid of fiducial markers. The optical measurements of the flow and the structure were conducted with a CVV probe mounted on a robotic arm, and both data sets were processed with the PTV algorithm Shake-the-Box. This integrated measurement approach requires minimal instrumentation of the wing model, and therefore provides a strategy that considerably simplifies the simultaneous measurement of the aerodynamic and structural response in aeroelastic experiments.

After applying custom postprocessing procedures for the particle tracks of the flow and structure separately, the three different forces in the aeroelastic interaction were determined from the results of the PTV measurements using three different methods. The inertial force was determined as the product of mass and acceleration, whereas the aerodynamic force was determined with an unsteady potential flow model, and the elastic force was determined with a finite element beam model. The physical agreement between the forces from the three models was similar to the agreement between the elastic force and the reference data from the balance measurements, which supports the results for the aerodynamic and inertial forces, and indicates that the structural model should be calibrated with additional structural measurements of the wing, to achieve a better characterization result.

In this demonstration study, physical models of relatively low complexity were used to determine the forces from the measurement data. However, the complexity of the aerodynamic and structural models that are used to analyze the measurements, which are obtained with the considered integrated measurement approach, could be increased if required. This would be necessary in particular in the case of nonlinear aerodynamic effects due to flow separation, or large structural deformations that cannot be modeled with the linear theory of small deflections.

Acknowledgment

This work has been carried out in the context of the HOMER (Holistic Optical Metrology for Aero-Elastic Research) project that has received funding from the European Union's Horizon 2020 research and innovation programme under grant agreement No. 769237.

References

[1] Collar, A. R., "The Expanding Domain of Aeroelasticity," *Aeronautical Journal*, Vol. 50, No. 428, 1946, pp. 613–636.
[2] Pike, E. C., "Manual on Aeroelasticity," AGARD, Rept. 578, 1971.
[3] Livne, E., "Future of Airplane Aeroelasticity," *Journal of Aircraft*, Vol. 40, No. 6, 2003, pp. 1066–1092. https://doi.org/10.2514/2.7218
[4] Tang, D., and Dowell, E., "Experimental Aeroelastic Models Design and Wind Tunnel Testing for Correlation with New Theory," *Aerospace*,

Vol. 3, No. 2, 2016, pp. 1–25.
https://doi.org/10.3390/aerospace3020012.

[5] Raffel, M., Willert, C. E., Scarano, F., Kähler, C. J., Wereley, S., and Kompenhans, J., *Particle Image Velocimetry: A Practical Guide*, 3rd ed., Springer, Cham, Switzerland, 2018, Chap. 9.
https://doi.org/10.1007/978-3-319-68852-7.

[6] Pan, B., "Digital Image Correlation for Surface Deformation Measurement: Historical Developments, Recent Advances and Future Goals," *Measurement Science and Technology*, Vol. 29, No. 8, 2018, pp. 1–32.
https://doi.org/10.1088/1361-6501/aac55b

[7] Marimon Giovannetti, L., Banks, J., Turnock, S. R., and Boyd, S. W., "Uncertainty Assessment of Coupled Digital Image Correlation and Particle Image Velocimetry for Fluid-Structure Interaction Wind Tunnel Experiments," *Journal of Fluids and Structures*, Vol. 68, Jan. 2017, pp. 125–140.
https://doi.org/10.1016/j.jfluidstructs.2016.09.002

[8] Zhang, P., Peterson, S. D., and Porfiri, M., "Combined Particle Image Velocimetry/Digital Image Correlation for Load Estimation," *Experimental Thermal and Fluid Science*, Vol. 100, Jan. 2019, pp. 207–221.
https://doi.org/10.1016/j.expthermflusci.2018.09.011.

[9] Liu, T., Montefort, J., Gregory, J., Palluconi, S., Crafton, J., and Fonov, S., "Wing Deformation Measurements from Pressure Sensitive Paint Images Using Videogrammetry," *41st AIAA Fluid Dynamics Conference and Exhibit*, AIAA, Reston, VA, 2011, pp. 1–31.
https://doi.org/10.2514/6.2011-3725

[10] Schanz, D., Gesemann, S., and Schröder, A., "Shake-The-Box: Lagrangian Particle Tracking at High Particle Image Densities," *Experiments in Fluids*, Vol. 57, No. 5, 2016, pp. 1–27.
https://doi.org/10.1007/s00348-016-2157-1

[11] Scarano, F., Ghaemi, S., Caridi, G. C. A., Bosbach, J., Dierksheide, U., and Sciacchitano, A., "On the Use of Helium-Filled Soap Bubbles for Large-Scale Tomographic PIV in Wind Tunnel Experiments," *Experiments in Fluids*, Vol. 56, No. 2, 2015, pp. 1–12.
https://doi.org/10.1007/s00348-015-1909-7

[12] Huhn, F., Schanz, D., Gesemann, S., Dierksheide, U., van de Meerendonk, R., and Schröder, A., "Large-Scale Volumetric Flow Measurement in a Pure Thermal Plume by Dense Tracking of Helium-Filled Soap Bubbles," *Experiments in Fluids*, Vol. 58, No. 9, 2017, pp. 1–19.
https://doi.org/10.1007/s00348-017-2390-2

[13] Martínez Gallar, B., van Oudheusden, B. W., Sciacchitano, A., and Karásek, M., "Large-Scale Volumetric Flow Visualization of the Unsteady Wake of a Flapping-Wing Micro Air Vehicle," *Experiments in Fluids*, Vol. 61, No. 1, 2019, pp. 1–21.
https://doi.org/10.1007/s00348-019-2854-7

[14] Wolf, C. C., Schwarz, C., Kaufmann, K., Gardner, A. D., Michaelis, D., Bosbach, J., Schanz, D., and Schröder, A., "Experimental Study of Secondary Vortex Structures in a Rotor Wake," *Experiments in Fluids*, Vol. 60, No. 11, 2019, pp. 1–16.
https://doi.org/10.1007/s00348-019-2807-1

[15] Mitrotta, F. M. A., Sciacchitano, A., Sodja, J., de Breuker, R., and van Oudheusden, B. W., "Experimental Investigation of the Fluid-Structure Interaction Between a Flexible Plate and a Periodic Gust by Means of Robotic Volumetric PIV," *13th International Symposium on Particle Image Velocimetry*, edited by C. J. Kähler, R. Hain, S. Scharnowski, and T. Fuchs, Universität der Bundeswehr München, Neubiberg, Germany, 2019, pp. 645–656.
https://doi.org/10.18726/2019_3

[16] van Oudheusden, B. W., "PIV-Based Pressure Measurement," *Measurement Science and Technology*, Vol. 24, No. 3, 2013, pp. 1–32.
https://doi.org/10.1088/0957-0233/24/3/032001

[17] Rival, D. E., and van Oudheusden, B. W., "Load-Estimation Techniques for Unsteady Incompressible Flows," *Experiments in Fluids*, Vol. 58, No. 3, 2017, pp. 1–0.
https://doi.org/10.1007/s00348-017-2304-3

[18] Gherlone, M., Cerracchio, P., and Mattone, M., "Shape Sensing Methods: Review and Experimental Comparison on a Wing-Shaped Plate," *Progress in Aerospace Sciences*, Vol. 99, May 2018, pp. 14–26.
https://doi.org/10.1016/j.paerosci.2018.04.001

[19] Anderson, J. D., Jr., *Fundamentals of Aerodynamics*, 5th ed., McGraw–Hill, New York, 2011, Chap. 3.

[20] Lind, A. H., Lefebvre, J. N., and Jones, A. R., "Time-Averaged Aerodynamics of Sharp and Blunt Trailing-Edge Static Airfoils in Reverse Flow," *AIAA Journal*, Vol. 52, No. 12, 2014, pp. 2751–2764.
https://doi.org/10.2514/1.J052967

[21] Lee, T., and Su, Y. Y., "Low Reynolds Number Airfoil Aerodynamic Loads Determination via Line Integral of Velocity Obtained with Particle Image Velocimetry," *Experiments in Fluids*, Vol. 53, No. 5, 2012, pp. 1177–1190.
https://doi.org/10.1007/s00348-012-1353-x

[22] Katz, J., and Plotkin, A., *Low-Speed Aerodynamics*, 2nd ed., Cambridge Univ. Press, New York, 2001, Chap. 13.

[23] Mitrotta, F. M. A., Rajpal, D., Sodja, J., and De Breuker, R., "Multi-Fidelity Design of an Aeroelastically Tailored Composite Wing for Dynamic Wind Tunnel Testing," *AIAA SciTech Forum*, AIAA, Reston, VA, 2020, pp. 1–26.
https://doi.org/10.2514/6.2020-1636

[24] Hodges, D. H., and Pierce, G. A., *Introduction to Structural Dynamics and Aeroelasticity*, 2nd ed., Cambridge Univ. Press, New York, 2011, Chap. 3.

[25] Lancelot, P. M. G. J., Sodja, J., Werter, N. P. M., and Breuker, R. D., "Design and Testing of a Low Subsonic Wind Tunnel Gust Generator," *Advances in Aircraft and Spacecraft Science*, Vol. 4, No. 2, 2017, pp. 125–144.
https://doi.org/10.12989/aas.2017.4.2.125

[26] Leishman, J. G., *Principles of Helicopter Aerodynamics*, 2nd ed., Cambridge Univ. Press, New York, 2006, Chap. 8.

[27] Faleiros, D. E., Tuinstra, M., Sciacchitano, A., and Scarano, F., "Generation and Control of Helium-Filled Soap Bubbles for PIV," *Experiments in Fluids*, Vol. 60, No. 3, 2019, pp. 1–17.
https://doi.org/10.1007/s00348-019-2687-4.

[28] Schneiders, J. F. G., Scarano, F., Jux, C., and Sciacchitano, A., "Coaxial Volumetric Velocimetry," *Measurement Science and Technology*, Vol. 29, No. 6, 2018, pp. 1–15.
https://doi.org/10.1088/1361-6501/aab07d

[29] Jux, C., Sciacchitano, A., Schneiders, J. F. G., and Scarano, F., "Robotic Volumetric PIV of a Full-Scale Cyclist," *Experiments in Fluids*, Vol. 59, No. 4, 2018, pp. 1–15.
https://doi.org/10.1007/s00348-018-2524-1

[30] Schanz, D., Gesemann, S., Schröder, A., Wieneke, B., and Novara, M., "Non-Uniform Optical Transfer Functions in Particle Imaging: Calibration and Application to Tomographic Reconstruction," *Measurement Science and Technology*, Vol. 24, No. 2, 2013, pp. 1–15.
https://doi.org/10.1088/0957-0233/24/2/024009

[31] Sciacchitano, A., and Scarano, F., "Elimination of PIV Light Reflections via a Temporal High Pass Filter," *Measurement Science and Technology*, Vol. 25, No. 8, 2014, pp. 1–13.
https://doi.org/10.1088/0957-0233/25/8/084009

[32] Wieneke, B., "Volume Self-Calibration for 3D Particle Image Velocimetry," *Experiments in Fluids*, Vol. 45, No. 4, 2008, pp. 549–556.
https://doi.org/10.1007/s00348-008-0521-5

[33] Agüera, N., Cafiero, G., Astarita, T., and Discetti, S., "Ensemble 3D PTV for High Resolution Turbulent Statistics," *Measurement Science and Technology*, Vol. 27, No. 12, 2016, pp. 1–12.
https://doi.org/10.1088/0957-0233/27/12/124011

A. R. Jones
Associate Editor

This article has been cited by:

1. Christoph Mertens, Jurij Sodja, Andrea Sciacchitano, Bas van Oudheusden. Experimental Aeroelastic Characterization of a Very Flexible Wing in Steady and Unsteady Inflow . [Abstract] [PDF] [PDF Plus]